九州大学大学院総合理工学府報告
第 45 巻 1 号 13-24 頁 令和 5 年 9 月

Engineering Sciences Reports, Kyushu University
Vol. 45, No. 1, pp. 13-24, SEP, 2023

Spin-orbit State Selectivity in the Formation of RgCl(B,C,D) Excimers from Ion-Ion Recombination Reactions of Rg^+ with $C_6F_5Cl^-$ in the Flowing Afterglow

Masaharu TSUJI,[*1,2†] Hiroaki ISHIMI,[*3] Keiko UTO,[*1]
Jun-Ichiro HAYASHI[*1] and Takeshi TSUJI[*4]
[†]E-mail of corresponding author: tsuji@cm.kyushu-u.ac.jp

(Received March 27, 2023, accepted April 18, 2023)

RgCl(B,C,D) excimers were produced for Rg = Ar, Kr, and Xe by the positive ion-negative ion recombination reactions of $Rg^+(^2P_{1/2,3/2})$ with $C_6F_5Cl^-$ in the flowing afterglow. Spin-orbit state selectivity of RgCl(B,C,D) excimers by the $Rg^+(^2P_{1/2})$ and $Rg^+(^2P_{3/2})$ components was examined by using appropriate filter gases of one spin-orbit component. The RgCl(B,D) ratio was determined to be 0.35:0.65, 0.05:0.95, and 0.24:0.76 in the $Ag^+(^2P_{1/2})$, $Kr^+(^2P_{1/2})$, and $Xe^+(^2P_{1/2})$ reactions, whereas the RgCl(B,C) ratio was estimated to be 0.74:0.26, 0.71:0.29, and 0.70:0.30 in the $Ag^+(^2P_{3/2})$, $Kr^+(^2P_{3/2})$, and $Xe^+(^2P_{3/2})$ reactions, respectively. The $Rg^+(^2P_{1/2})$ reactions had a high propensity to give RgCl(D) plus a lesser amount of RgCl(B), whereas the $Rg^+(^2P_{3/2})$ reactions gave only RgCl(B,C). These results show that $Rg^+(^2P_{1/2}) + Cl^-$ and $Rg^+(^2P_{3/2}) + Cl^-$ characters are conserved well for the formation of RgCl* in the ion-ion recombination reactions between $Rg^+(^2P_{1/2,3/2})$ and $C_6F_5Cl^-$. Higher conservation of $Rg^+(^2P_{1/2})$ character in the $Rg^+(^2P_{1/2})/C_6F_5Cl^-$ reactions than that in the $Rg(^3P_0)$/halides reactions is discussed by using correlation diagram between entrance and exit product channels.

Key words: *Positive ion-negative ion reaction, Recombination reaction, RgCl* excimer, Ar^+, Kr^+, Xe^+, $C_6F_5Cl^-$, Flowing afterglow, Emission spectroscopy, Spin-orbit state selectivity, Correlation diagram*

1. Introduction

We have successfully applied the flowing afterglow apparatus to the study on two-body dissociative ionic-recombination reactions[1-4)]

$$Rg^+(^2P_{1/2,3/2}) + SF_6^- \rightarrow RgF(B,C,D) + SF_5, \quad (1)$$

where Rg represents Ar, Kr, or Xe atom. Positive $Rg^+(^2P_{1/2,3/2})$ ions were formed by $He(2^3S)$/Rg Penning ionization and negative SF_6^- ions were produced by attachment of Penning electrons to SF_6. The spin-orbit state selectivity in the KrF* and XeF* formation was examined by selecting one of the spin-orbit components of Kr^+ and Xe^+, $^2P_{1/2}$ or $^2P_{3/2}$. It was found that Kr^+ and Xe^+ ions in the $^2P_{1/2}$ level preferentially give the D state, while those in the $^2P_{3/2}$ level give only the B and C states. The high spin-orbit state selectivity was explained by the conservation of $Rg^+(^2P_{1/2}) + F^-$ and $Rg^+(^2P_{3/2}) + F^-$ characters.

In this study, ion-ion recombination reactions of $Ar^+(^2P_{1/2,3/2})$, $Kr^+(^2P_{1/2,3/2})$, and $Xe^+(^2P_{1/2,3/2})$ with $C_6F_5Cl^-$ are studied by observing RgCl* excimer emissions in the flowing afterglow. By using various filter gases of one spin-orbit component, effects of spin-orbit state are examined. Results obtained are compared with previous data for the formation of RgX* (X = halogen) excimers from the ion-ion recombination reactions of $Rg^+(^2P_{1/2,3/2})/SF_6^-$ (Rg = Kr, Xe)[2)] and from energy-transfer reactions of $Ar(^3P_{0,2})$ with simple halides.[5-7)]

2. Experimental

2.1 Chemicals

Rare gases, filter gases used for spin-orbit state selection, and an electron scavenger C_6F_5Cl used in this study were obtained from

*1 Institute for Materials Chemistry and Engineering, and Research and Education Center of Green Technology
*2 Department of Molecular Science and Technology
*3 Department of Molecular Science and Technology, Graduate Student
*4 Department of Materials Science, Shimane University

Japanese chemical companies: He (purity >99.9999%, Taiyo Sanso), Ar (99.999%, Nippon Sanso), Kr (99.995%, Nippon Sanso), Xe (99.99%, Nippon Sanso), N_2 (99.9999%, Taiyo Sanso), O_2 (99.9%, Nippon Sanso), C_2H_2 (99%, Eto Sanso), CH_4 (99.9%, Nippon Sanso), and C_6F_5Cl (Kishida Kagaku, 95%). These reagents were used without further purification.

2.2 Flowing-afterglow apparatus and experimental procedure

Two-types of flowing-afterglow experiments were carried out for the $Ar^+(^2P_{1/2,3/2})$ reactions. One is an Ar afterglow experiment shown in Fig. 1(a), whereas the other is a He afterglow experiment shown in Fig. 1(b).

In the Ar afterglow experiment, such Ar active species as metastable $Ar(^3P_{0,2})$ atoms and Ar^+ ions were generated by a microwave discharge of Ar gas at the output power of 80 W, and the C_6F_5Cl gas was introduced from the second gas inlet placed 20 cm downstream from the center of microwave discharge. Effects of charged particles were examined by using a pair of charged-particle collector grids placed between the discharge section and the reaction zone. The partial pressures in the reaction zone were 0.18–1.0 Torr (1 Torr = 133.33 Pa) for Ar and 3–5 mTorr for C_6F_5Cl.

In the He afterglow experiment such He active species as $He(2^3S)$, He^+, and He_2^+ were generated by a microwave discharge of high purity He gas at the output power of 70 W. He^+ and He_2^+ ions in the discharge flow were trapped by using charged-particle collector grids. Therefore, only neutral $He(2^3S)$ atoms can arrive at the reaction zone as He active species. A small amount of Ar gas was added to the He flow 10 cm downstream from the center of microwave discharge. The positive $Ar^+(^2P_{1/2,3/2})$ ion was produced by the $He(2^3S)$/Ar, Penning ionization.

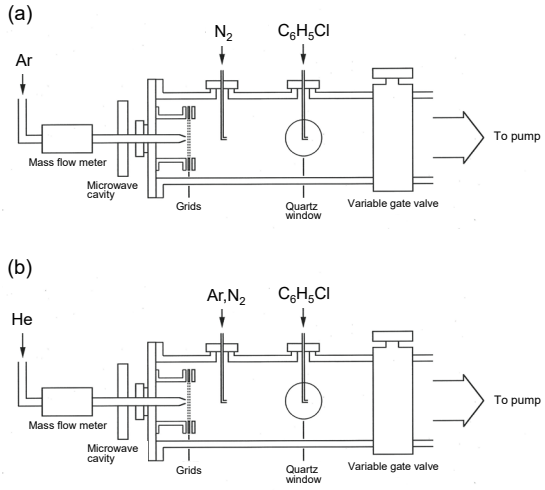

Fig. 1. (a) Ar and (b) He flowing-afterglow apparatuses for the study on the $Ar^+(^2P_{1/2,3/2})/C_6F_5Cl^-$ ion-ion recombination reaction. N_2 was added as a filter gas of the $Ar^+(^2P_{1/2})$ component.

$$He(2^3S) + Ar \rightarrow Ar^+(^2P_{1/2,3/2}) + He + e^-. \quad (2)$$
$$(k_2 = 7.04 \times 10^{-11}\ cm^3\ s^{-1}\ [Ref.\ 8])$$

An electron attachment gas, C_6F_5Cl, was added from the second gas inlet, where $C_6F_5Cl^-$ ion was formed by a fast non-dissociative electron attachment.

$$C_6F_5Cl + e^- \rightarrow C_6F_5Cl^-. \quad (3)$$
$$(k_3 = 1.0 \times 10^{-7}\ cm^3\ s^{-1}\ [Ref.\ 9])$$

$Kr^+(^2P_{1/2,3/2})$ and $Xe^+(^2P_{1/2,3/2})$ reactions were carried out using similar He afterglow apparatus. In these cases, $Kr^+(^2P_{1/2,3/2})$ and $Xe^+(^2P_{1/2,3/2})$ ions were formed by $He(2^3S)$/Kr and $He(2^3S)$/Xe Penning ionization, respectively.

$$He(2^3S) + Kr \rightarrow Kr^+(^2P_{1/2,3/2}) + He + e^-. \quad (4)$$
$$(k_4 = 9.94 \times 10^{-11}\ cm^3\ s^{-1}\ [Ref.\ 8])$$

$$He(2^3S) + Xe \rightarrow Xe^+(^2P_{1/2,3/2}) + He + e^-. \quad (5)$$
$$(k_5 = 1.24 \times 10^{-10}\ cm^3\ s^{-1}\ [Ref.\ 8])$$

The partial pressures in the reaction zone were 1.0 Torr (1 Torr = 133.33 Pa) for He, 5–40 mTorr for Rg (Rg = Ar, Kr, and Xe), and 3–5 mTorr for C_6F_5Cl. The greatest advantage of the He afterglow experiment is that we can save expensive rare gases, Kr and Xe for the $Kr^+(^2P_{1/2,3/2})$ and $Xe^+(^2P_{1/2,3/2})$ reactions.

When the effects of incident spin-orbit states in $Ar^+(^2P_{1/2,3/2})$, $Kr^+(^2P_{1/2,3/2})$, and $Xe^+(^2P_{1/2,3/2})$ were examined, one of the spin-orbit states was isolated before reaching the second gas inlet. For the isolation of $Ar^+(^2P_{3/2})$, $Kr^+(^2P_{1/2})$, $Xe^+(^2P_{1/2})$, and $Xe^+(^2P_{3/2})$, N_2, O_2, C_2H_2, and CH_4 were used as filter gases, respectively, because the quenching rate constants of the $^2P_{1/2}$ and $^2P_{3/2}$ states are different at least one order of magnitude.

$$Ar^+(^2P_{1/2}) + N_2 \rightarrow Ar^+(^2P_{3/2}) + N_2, \quad (6a)$$
$$(k_{6a} = 3.2 \times 10^{-11}\ cm^3\ s^{-1}\ [Ref.\ 10])$$
$$Ar^+(^2P_{1/2}) + N_2 \rightarrow N_2^+ + Ar, \quad (6b)$$
$$(k_{6b} = 3.8 \times 10^{-11}\ cm^3\ s^{-1}\ [Ref.\ 10])$$

$Ar^+(^2P_{3/2}) + N_2 \rightarrow N_2^+ + Ar.$ (6c)
($k_{6c} = 3.7 \times 10^{-12}$ cm^3 s^{-1} [Ref. 10])

$Kr^+(^2P_{1/2}) + O_2 \rightarrow$ no products, (7a)
($k_{7a} \leq 1 \times 10^{-12}$ cm^3 s^{-1} [Ref. 11])

$Kr^+(^2P_{3/2}) + O_2 \rightarrow O_2^+ + Kr.$ (7b)
($k_{7b} = 4.7 \times 10^{-11}$ cm^3 s^{-1} [Ref. 11])

$Xe^+(^2P_{1/2}) + C_2H_2 \rightarrow C_2H_2^+ + Xe,$ (8a)
($k_{8a} = 3.5 \times 10^{-11}$ cm^3 s^{-1} [Ref. 11])

$Xe^+(^2P_{3/2}) + C_2H_2 \rightarrow C_2H_2^+ + Xe.$ (8b)
($k_{8b} = 5.0 \times 10^{-10}$ cm^3 s^{-1} [Ref. 11])

$Xe^+(^2P_{3/2}) + CH_4 \rightarrow CH_4^+ + Xe,$ (9a)
($k_{9a} = 9.0 \times 10^{-10}$ cm^3 s^{-1} [Ref. 11])

$Xe^+(^2P_{1/2}) + CH_4 \rightarrow$ no products. (9b)
($k_{9b} \leq 1 \times 10^{-12}$ cm^3 s^{-1} [Ref. 11])

These filter gases were injected from the first gas inlet, as shown in Figs (1a) and (1b) for the case of N_2 in the $Ar^+(^2P_{1/2,3/2})/C_6F_5Cl^-$ reaction. The partial pressures of the filter gases were 10–200 mTorr.

The emission spectra, observed around the C_6F_5Cl gas inlet, were dispersed in the 120–840 nm region with McPherson 218 and Spex 1250M monochromators. Photon signals from a cooled photomultiplier were analyzed with a microcomputer.

We used ionization potentials of Ar, Kr, Xe, and C_6F_5Cl, electron affinity of C_6F_5Cl, dissociation energy of D(C_6F_5–Cl), excitation energies of RgCl* reported in Refs. 12–18 for the calculations of energetics in each reaction.

3. Results and Discussion

3.1 Formation of ArCl* excimer from the $Ar^+(^2P_{1/2,3/2})/C_6F_5Cl^-$ reaction in the Ar and He afterglow

Figures 2(a)–2(d) show emission spectra of C_6F_5Cl in an Ar flowing afterglow at various Ar gas pressures. At the lowest Ar pressure of 0.18 Torr, very weak unidentified atomic lines are observed. At higher Ar gas pressures of 0.42–1.0 Torr, three transitions of ArCl* excimer and Cl* lines are identified in the 130–210 nm region. The intensities of ArCl* and Cl* increase with increasing the Ar pressure from 0.42 Torr to 0.68 Torr, and then decrease with further increasing Ar pressure from 0.68 Torr to 1.0 Torr. ArCl* excimer bands, on which present work focuses, consists of the strong B(1/2)–X(1/2) transition in the 160–180 nm region, the weak D(1/2)–X(1/2) transition in the 140–173 nm region, and the weak broad C(3/2)–A(3/2) transition in the 180–207 nm region. Since the B, C, and D states of RgX* are strongly bound, whereas the X and A states of RgX* are repulsive,[16-18] continuous bands without vibrational structures are observed for the ArCl(B–X, D–X, C–A) bound-free transitions.

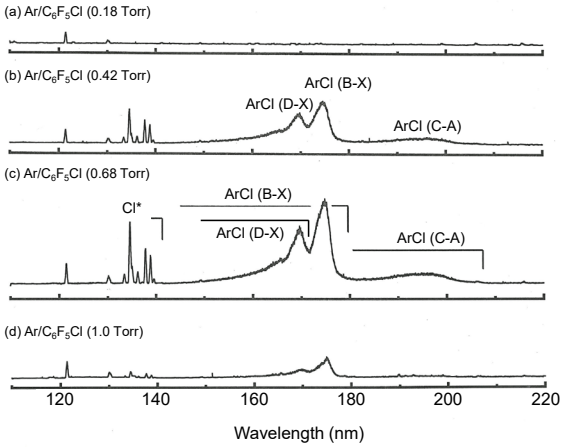

Fig. 2. Emission spectra resulting from the $Ar^+(^2P_{1/2,3/2})/C_6F_5Cl^-$ reaction in the 110–220 nm region at various Ar gas pressures.

Possible excitation sources of ArCl* emissions are metastable $Ar(^3P_2)$ and $Ar(^3P_0)$ atoms and $Ar^+(^2P_{3/2})$ and $Ar^+(^2P_{1/2})$ ions. The energetics for the formation of ArCl(B,C,D) from the $Ar(^3P_{0,2})/C_6F_5Cl$ and $Ar^+(^2P_{1/2,3/2})/C_6F_5Cl^-$ reaction is as follows:

$Ar(^3P_2) + C_6F_5Cl$
$\rightarrow ArCl(B) + C_6F_5 + 0.58$ eV, (10a)
$\rightarrow ArCl(C) + C_6F_5 + 0.48$ eV, (10b)
$\rightarrow ArCl(D) + C_6F_5 + 0.28$ eV. (10c)

$Ar(^3P_0) + C_6F_5Cl$
$\rightarrow ArCl(B) + C_6F_5 + 0.75$ eV, (11a)
$\rightarrow ArCl(C) + C_6F_5 + 0.65$ eV, (11b)
$\rightarrow ArCl(D) + C_6F_5 + 0.45$ eV. (11c)

$Ar^+(^2P_{3/2}) + C_6F_5Cl^-$
$\rightarrow ArCl(B) + C_6F_5 + 4.04$ eV, (12a)
$\rightarrow ArCl(C) + C_6F_5 + 3.94$ eV, (12b)
$\rightarrow ArCl(D) + C_6F_5 + 3.74$ eV. (12c)

$Ar^+(^2P_{1/2}) + C_6F_5Cl^-$
$\rightarrow ArCl(B) + C_6F_5 + 4.22$ eV, (13a)
$\rightarrow ArCl(C) + C_6F_5 + 4.12$ eV, (13b)
$\rightarrow ArCl(D) + C_6F_5 + 3.92$ eV. (13c)

Based on energetics, both metastable $Ar(^3P_{0,2})$ atoms and $Ar^+(^2P_{3/2,1/2})$ ions can be excitation

sources of ArCl*. Figures 3(a) and 3(b) show emission spectra at an Ar pressure of 0.68 Torr without and after ion trapping using ion collector grids, respectively. ArCl* and Cl* emissions disappear almost completely in Fig. 3(b), indicating that only charged $Ar^+(^2P_{3/2,1/2})$ ions take part in the formation of ArCl* and Cl* at 0.68 Torr.

In order to further confirm the excitation source of ArCl* emission in the Ar flowing afterglow, the Ar pressure dependence of ArCl(B–X) emission was compared with those of N_2(C–B) emission due to the $Ar(^3P_{0,2})/N_2$ reaction[19,20] and ArF(B–X) emission due to the $Ar^+(^2P_{1/2,3/2})/SF_6^-$ reaction (Fig. 4).[1,2]

$$Ar(^3P_{0,2}) + N_2 \rightarrow N_2(C) + Ar. \quad (14)$$
$$Ar^+(^2P_{1/2,3/2}) + SF_6^- \rightarrow ArF(B) + SF_5. \quad (15)$$

The ArCl(B–X) and ArF(B–X) bands by the $Ar^+(^2P_{1/2,3/2})$ reaction appeared at an Ar pressure of ~0.2 Torr with a single intensity peak at ~0.65 Torr, while the N_2(C–B) band by the $Ar(^3P_{0,2})/N_2$ reaction appeared at a lower Ar pressure of ~0.05 Torr with two intensity peaks at 0.15 and 0.7 Torr. A similar Ar pressure dependence between ArCl(B–X) and ArF(B–X) emissions suggests that ArCl(B) excimer is formed by the $Ar^+(^2P_{1/2,3/2})$ reaction. An important finding in this work is that product channels leading to ArCl(B,C,D) excimers, processes (10) and (11), are closed in the $Ar(^3P_{0,2})/C_6F_5Cl$ reaction, even though they are energetically allowed.

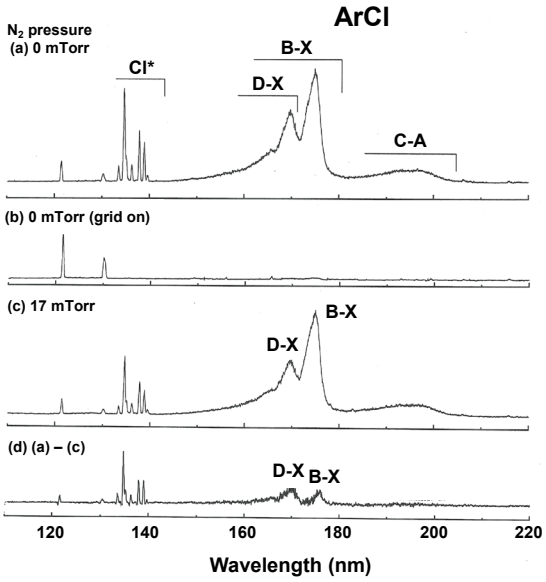

Fig. 3. Emission spectra resulting from the (a) $Ar^+(^2P_{1/2,3/2})/C_6F_5Cl^-$ reaction in the Ar afterglow, (b) ion-collection in spectrum (a), (c) by the addition of 17 mTorr of N_2, and (d) $Ar^+(^2P_{1/2})/C_6F_5Cl^-$ reaction. Spectrum (d) was obtained by subtracting spectrum (c) from spectrum (a).

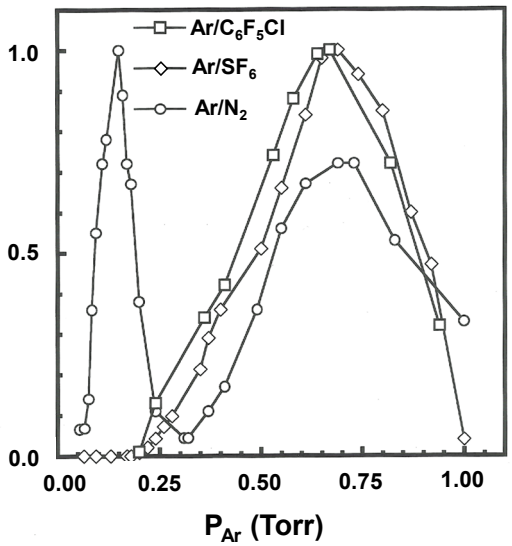

Fig. 4. Dependence of emission intensities of ArCl(B–X) band from the $Ar^+/C_6F_5Cl^-$ reaction, ArF(B–X) band from the Ar^+/SF_6^- reaction, and N_2(C–B) band from the $Ar(^3P_{0,2})/N_2$ reaction in the Ar flowing afterglow.

Figure A1 in Appendix shows effects of N_2 addition on the emission spectra of ArCl* resulting from the $Ar^+(^2P_{1/2,3/2})/C_6F_5Cl^-$ reaction. With increasing the N_2 pressure, the $[Ar^+(^2P_{3/2})]/[Ar^+(^2P_{1/2})]$ ratio is expected to be enhanced. Without addition of N_2 (Fig. A1(a)), the weak ArCl(D–X) band appears as a shoulder band of the main ArCl(B–X) band, and the weak broad ArCl(C–A) band is observed in the longer wavelength region of the ArCl(B–X) band. With increasing the partial pressure of N_2 from 21 mTorr to 93 mTorr (Fig. A1(b)–1(e)), the intensity of ArCl(D–X) band decreases more rapidly than those of ArCl(B–X) and ArCl(C–A) bands, and the ArCl(D–X) band almost disappears at the highest N_2 pressure of 140 mTorr (Fig. A1(f)). This shows that the ArCl(D–X) band is produced from the $Ar^+(^2P_{1/2})/C_6F_5Cl^-$ reaction, whereas ArCl(B–X) and ArCl(C–A) bands arise from the $Ar^+(^2P_{3/2})/C_6F_5Cl^-$ reaction.

A similar disappearance of the ArCl(D–X) band by the N_2 addition is found in the $Ar^+(^2P_{1/2,3/2})/C_6F_5Cl^-$ reaction in the He

afterglow (Fig. A2(a)–2(d) in Appendix). With increasing the N_2 pressure, ArCl(D–X) band decreases more rapidly than those of ArCl(B–X,C–A) bands, and it nearly disappears at N_2 pressure of 19 mTorr. From the intensity ratio between the ArCl(B–X) and ArCl(C–A) bands in the Ar and He afterglow, the branching ratio of ArCl(B) and ArCl(C) in processes (12a) and (12b) was estimated to be 0.74:0.26, respectively.

Figure 3(c) shows emission spectrum of C_6F_5Cl in the Ar flowing afterglow after addition of 17 mTorr of N_2. ArCl(B–X,C–A,D–X) emissions reduced their intensities in comparison with those in Fig. 3(a) obtained without N_2 addition. Decay rate of $Ar^+(^2P_{1/2})$ is about 20 times faster than that of $Ar^+(^2P_{3/2})$ by the N_2 addition. Thus, we examined the contribution of the $Ar^+(^2P_{1/2})$ reaction by assuming that ArCl* emission resulting only from the $Ar^+(^2P_{1/2})/C_6F_5Cl^-$ reaction is attenuated by the addition of a small amount of N_2 (17 mTorr). Figure 3(d) shows emission spectrum of the $Ar^+(^2P_{1/2})/C_6F_5Cl^-$ reaction obtained by subtracting spectrum (c) from spectrum (a). In Fig. 3(d), weak ArCl(B-X) and ArCl(D–X) bands are observed, and the intensity of the ArCl(D–X) band is stronger than that of the ArCl(B–X) one. From the intensity ratio of the two band systems, the branching ratio of ArCl(B) and ArCl(D) in processes (13a) and (13c) was estimated to be 0.35:0.65, respectively.

3.2 Formation of KrCl* excimer from the $Kr^+(^2P_{1/2,3/2})/C_6F_5Cl^-$ reaction in the He afterglow

Figure 5(a) shows emission spectrum resulting from the $Kr^+(^2P_{1/2,3/2})/C_6F_5Cl^-$ reaction in the He afterglow. The strong KrCl(B–X) band, the very weak KrCl(D–X) band, and the weak broad KrCl(C–A) band are identified in the 160–225, 160–200, and 225–275 nm region, respectively. Figures 5(b) and 5(c), respectively, show emission spectra obtained by addition of O_2 at partial pressures of 50 and 100 mTorr to enhance the $[Kr^+(^2P_{1/2})]/[Kr^+(^2P_{3/2})]$ ratio. With increasing the partial pressure of O_2, KrCl(D–X)/KrCl(B–X) intensity ratio increases. By the addition of a sufficient amount of O_2 (~200 mTorr), the KrCl(D–X)/KrCl(B–X) intensity ratio further increases and becomes constant, as shown in Fig. 5(d). Based on these experiments, the branching ratio of KrCl(B) and KrCl(C) in processes (16a) and (16b), and that of KrCl(B) and KrCl(D) in processes (17a) and (17c) were evaluated to be 0.71:0.29 and 0.05:0.95, respectively.

$$Kr^+(^2P_{3/2}) + C_6F_5Cl^- \rightarrow KrCl(B) + C_6F_5 + 3.67\ eV, \quad (16a)$$
$$\rightarrow KrCl(C) + C_6F_5 + 3.67\ eV, \quad (16b)$$
$$\rightarrow KrCl(D) + C_6F_5 + 3.05\ eV. \quad (16c)$$

$$Kr^+(^2P_{1/2}) + C_6F_5Cl^- \rightarrow KrCl(B) + C_6F_5 + 4.34\ eV, \quad (17a)$$
$$\rightarrow KrCl(C) + C_6F_5 + 4.34\ eV, \quad (17b)$$
$$\rightarrow KrCl(D) + C_6F_5 + 3.72\ eV. \quad (17c)$$

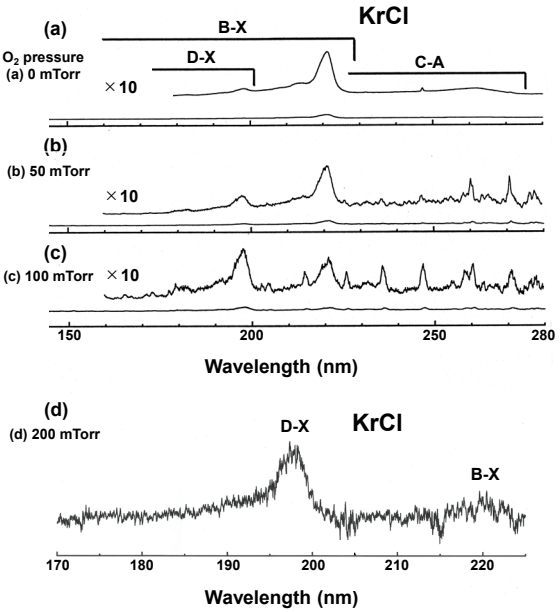

Fig. 5. Emission spectra resulting from the $Kr^+/C_6F_5Cl^-$ reaction in the 150–280 nm or 170–230 nm region. (a) without O_2 addition, (b) 50 mTorr O_2 addition, (c) 100 mTorr O_2 addition, (d) 200 mTorr O_2 addition.

3.3 Formation of XeCl* excimer from the $Xe^+(^2P_{1/2,3/2})/C_6F_5Cl^-$ reaction in the He afterglow

Figure 6(a) shows emission spectrum resulting from the $Xe^+(^2P_{1/2,3/2})/C_6F_5Cl^-$ reaction in the He afterglow. XeCl* excimer bands consist of the strong XeCl(B–X) band in the 250–320 nm region, the very weak XeCl(D–X) band in the 200–240 nm region, and the weak broad XeCl(C–A) band in the 320–450 nm region. Figures 6(b) and 6(c) show emission spectra obtained by selecting one-spin-orbit component using C_2H_2 or CH_4 filter gases, respectively. In the $Xe^+(^2P_{1/2})/C_6F_5Cl^-$ reaction shown in Fig. 6(b), the XeCl(B–X) band greatly reduces its intensity by removal of the $Xe^+(^2P_{3/2})$

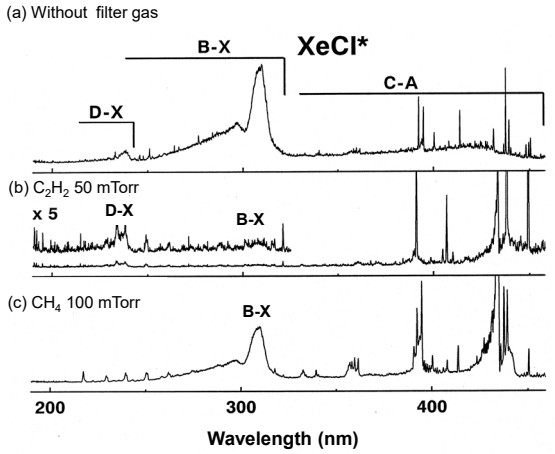

Fig. 6. Emission spectra resulting from the $Xe^+/C_6F_5Cl^-$ reaction in the 200–450 nm region. (a) $Xe^+(^2P_{1/2,3/2})/C_6F_5Cl^-$ reaction without addition of filter gas, (b) $Xe^+(^2P_{1/2})/C_6F_5Cl^-$ reaction by addition of 50 mTorr C_2H_2, (c) $Xe^+(^2P_{3/2})/C_6F_5Cl^-$ reaction by addition of 100 mTorr CH_4.

component, whereas the XeCl(D–X) band remains its intensity. On the other hand, in the $Xe^+(^2P_{3/2})/C_6F_5Cl^-$ reaction shown in Fig. 6(c), XeCl(B–X) and XeCl(C–A) bands remain their intensities, whereas the XeCl(D–X) band disappears. The branching ratio of XeCl(B) and XeCl(C) in processes (18a) and (18b) and that of XeCl(B) and XeCl(D) in processes (19a) and (19c) were evaluated to be 0.70:0.30 and 0.24:0.76, respectively.

$$Xe^+(^2P_{3/2}) + C_6F_5Cl^- \rightarrow XeCl(B) + C_6F_5 + 3.15\ eV, \quad (18a)$$
$$\rightarrow XeCl(C) + C_6F_5 + 3.08\ eV, \quad (18b)$$
$$\rightarrow XeCl(D) + C_6F_5 + 1.80\ eV. \quad (18c)$$

$$Xe^+(^2P_{1/2}) + C_6F_5Cl^- \rightarrow XeCl(B) + C_6F_5 + 4.46\ eV, \quad (19a)$$
$$\rightarrow XeCl(C) + C_6F_5 + 4.71\ eV, \quad (19b)$$
$$\rightarrow XeCl(D) + C_6F_5 + 3.11\ eV. \quad (19c)$$

3.4 Branching ratios of RgX(B,C,D) excimers in the ion-ion recombination reactions and chemiluminescent reactions

In Table 1 are summarized the branching ratios of RgX(B,C,D) excimers in the $Rg^+(^2P_{1/2})/C_6F_5Cl^-$ and $Rg^+(^2P_{3/2})/C_6F_5Cl^-$ reactions. For comparison, corresponding data for the Rg^+/SF_6^- reactions and chemiluminescent reactions of metastable $Rg(^3P_{0,2})$ atoms with diatomic and polyatomic halides RX are also given.

The initial formation ratio of two spin-orbit components of Kr^+ and Xe^+, $[^2P_{1/2}]/[^2P_{3/2}]$, in the Penning ionization (4) and (5) was estimated to be 0.56 for Kr^+ and 0.49 for Xe^+ from the analysis of Penning ionization electron spectra.[21] We found previously that RgF(B–X) emissions are formed highly selectively by the $Rg^+(^2P_{3/2})/SF_6^-$ reactions, whereas RgF(D–X) emissions preferentially results from the $Rg^+(^2P_{1/2})/SF_6^-$ reactions for Rg = Kr and Xe.[2] Therefore, the $[Rg^+(^2P_{1/2})]/[Rg^+(^2P_{3/2})]$ ratios can be estimated by using intensity ratios of RgF(D–X)/RgF(B–X) excimers resulting from spin-orbit state selective $Rg^+(^2P_{1/2,3/2})/SF_6^-$ reactions, assuming that no significant difference exists between the rate constant for the formation of RgF(D) from the $Rg^+(^2P_{1/2})/SF_6^-$ reaction and that of RgF(B) from the $Rg^+(^2P_{3/2})/SF_6^-$ reaction. We found that the RgF(B–X) emission is much stronger than that of RgF(D–X) emissions, as reported previously.[2] It was therefore concluded that the lower $Rg^+(^2P_{3/2})$ state is major component in the present experiments, although a small amount of upper $Rg^+(^2P_{1/2})$ state is involved in all cases.

It is clear that the B and D states are formed by the $Rg^+(^2P_{1/2})/C_6F_5Cl^-$ reactions with the D state being strongly favored, whereas the B and C state are produced by the $Rg^+(^2P_{3/2})/C_6F_5Cl^-$ reactions with the branching ratio of about 7:3, respectively in all cases. The $\Gamma(D)$ values for the $Ar^+(^2P_{1/2})/C_6F_5Cl^-$ and $Xe^+(^2P_{1/2})/C_6F_5Cl^-$ reactions, 0.65 and 0.76, respectively, are smaller than that for the $Kr^+(^2P_{1/2})/C_6F_5Cl^-$ reaction, 0.95. The $\Gamma(D)$ value for the $Kr^+(^2P_{1/2})/C_6F_5Cl^-$ reaction, 0.95, is the same as that for the $Kr^+(^2P_{1/2})/SF_6^-$ reaction, whereas the $\Gamma(D)$ value for the $Xe^+(^2P_{1/2})/C_6F_5Cl^-$ reaction, 0.76, is smaller than that for the $Xe^+(^2P_{1/2})/SF_6^-$ reaction, 0.94.

In the chemiluminescent reactions of metastable $Ar(^3P_{0,2})$ and $Kr(^3P_{0,2})$ atoms with halides RX, spin-orbit selectivity is also found. In these cases, $Ar(^3P_2)$ and $Kr(^3P_2)$ reactions give only B and C states, whereas mixtures of B and D states are formed in the $Ar(^3P_0)$ and $Kr(^3P_0)$ reactions. The $\Gamma(D)$ values in the $Ar(^3P_0)$ and $Kr(^3P_0)$ reactions range from 0.23 to 0.73, which are about the same or smaller than those obtained in the $Rg^+(^2P_{1/2})/C_6F_5Cl^-$ reactions (0.65–0.95). It should be noted that a significant difference is observed in the spin-orbit selectivity between the $Xe(^3P_0)/RX$ and the $Xe^+(^2P_{1/2})/C_6F_5Cl^-$ reactions. In strong contrast to the $Ar(^3P_0)$ and $Kr(^3P_0)$ reactions,

Table 1. Branching ratios of RgX(B,C,D) excimers in ion-ion recombination reactions and chemiluminescent (CL) reactions.

Ion-ion reactions		Γ(B)	Γ(C)	Γ(D)
$Ar^+(^2P_{1/2})/C_6F_5Cl^-$	This work	0.35		0.65
$Ar^+(^2P_{3/2})/C_6F_5Cl^-$	This work	0.74	0.26	
$Kr^+(^2P_{1/2})/C_6F_5Cl^-$	This work	0.05		0.95
$Kr^+(^2P_{3/2})/C_6F_5Cl^-$	This work	0.71	0.29	
$Xe^+(^2P_{1/2})/C_6F_5Cl^-$	This work	0.24		0.76
$Xe^+(^2P_{3/2})/C_6F_5Cl^-$	This work	0.70	0.30	
$Kr^+(^2P_{1/2})/SF_6^-$	Ref. 2	0.05		0.95
$Kr^+(^2P_{3/2})/SF_6^-$	Ref. 2	0.62	0.38	
$Xe^+(^2P_{1/2})/SF_6^-$	Ref. 2	0.06		0.94
$Xe^+(^2P_{3/2})/SF_6^-$	Ref. 2	0.68	0.32	

CL Reaction		Γ(B)	Γ(C)	Γ(D)
$Ar(^3P_0)/Cl_2$	Ref. 5	0.52	0.13	0.35
$Ar(^3P_2)/Cl_2$	Ref. 5	0.70	0.30	
$Ar(^3P_0)/SOCl_2$	Ref. 5	0.40	0.09	0.51
$Ar(^3P_2)/SOCl_2$	Ref. 5	0.69	0.31	
$Ar(^3P_0)/PCl_3$	Ref. 5	0.23	0.04	0.73
$Ar(^3P_2)/PCl_3$	Ref. 5	0.27	0.73	
$Ar(^3P_0)/CCl_4$	Ref. 5	0.26	0.08	0.66
$Ar(^3P_2)/CCl_4$	Ref. 5	0.33	0.67	
$Ar(^3P_0)/F_2$	Ref. 5	0.49	0.28	0.23
$Ar(^3P_2)/F_2$	Ref. 5	0.50	0.50	
$Kr(^3P_0)/Cl_2$	Ref. 6	0.42		0.58
$Kr(^3P_2)/Cl_2$	Ref. 6	0.52	0.48	
$Kr(^3P_0)/SOCl_2$	Ref. 6	0.46		0.54
$Kr(^3P_2)/SOCl_2$	Ref. 6	0.60	0.40	
$Kr(^3P_0)/PCl_3$	Ref. 8	1.00		
$Kr(^3P_2)/PCl_3$	Ref. 6	0.33	0.67	
$Kr(^3P_0)/CCl_4$	Ref. 6	0.50		0.50
$Kr(^3P_2)/CCl_4$	Ref. 8	0.40	0.60	
$Xe(^3P_0)/F_2$	Ref. 7	≥0.90		≤0.10
$Xe(^3P_2)/F_2$	Ref. 7	1.00 (B + C)		
$Xe(^3P_0)/Br_2$[a)]	Ref. 7	≥0.75		≤0.25
$Xe(^3P_2)/Br_2$	Ref. 7	1.00 (B + C)		
$Xe(^3P_0)/Cl_2$	Ref. 7	1.00 (B + C)		
$Xe(^3P_2)/Cl_2$	Ref. 7	1.00 (B + C)		
$Xe(^3P_0)/HCl$	Ref. 7	1.00 (B + C)		
$Xe(^3P_2)/HCl$	Ref. 7	1.00 (B + C)		
$Xe(^3P_0)/PCl_3$	Ref. 7	1.00 (B + C)		
$Xe(^3P_2)/PCl_3$	Ref. 7	1.00 (B + C)		
$Xe(^3P_0)/CF_3Cl$	Ref. 7	1.00 (B + C)		
$Xe(^3P_2)/CF_3Cl$	Ref. 7	1.00 (B + C)		

[a)] From peak intensity.

the Γ(D) values in the $Xe(^3P_0)$/RX reactions are zero except for F_2 (≤0.10) and Br_2 (≤0.25). The Γ(B) + Γ(C) values in the $Xe(^3P_2)$/RX reactions are 1.00 for all reagents, as in the cases of the $Ar(^3P_2)$ and $Kr(^3P_2)$ reactions and the $Xe^+(^2P_{3/2})/C_6F_5Cl^-$ reaction.

3.3 Reaction dynamics for the formation of RgCl(B,C,D) excimers in the reactions of $Rg^+(^2P_{1/2,3/2})$ with $C_6F_5Cl^-$

The formation of RgCl* excimers from the $Rg^+/C_6F_5Cl^-$ reactions must proceed through the $[Rg^+–Cl^–C_6F_5]$ intermediates.

$$Rg^+ + C_6F_5Cl^- \rightarrow [Rg^+–Cl^–C_6F_5] \rightarrow RgCl^* + C_6F_5. \quad (20)$$

The formation dynamics of RgX* excimers from the $Rg(^3P_{0,2})/X_2$ reaction using a correlation diagram is shown in Fig. A3 (Appendix), where RgX* excimers are formed through $Rg^+(^2P_{1/2,3/2})$ + X_2^- ion-pairs intermediates. It is known that changing the designation of the states to C_s geometry for RX^- molecules with A' or A'' symmetry does not alter the broad interpretation for X_2^- with higher symmetry.[5-7] Figure 7 shows the schematic potential diagram of the $Rg^+(^2P_{1/2,3/2})/C_6F_5Cl^-$ recombination process, where the Ω designation given in Fig. A3 remains for the $Rg(^3P_{0,2},^3P_1)$ + C_6F_5Cl, $Rg^+(^2P_{1/2,3/2})$ + $C_6F_5Cl^-$, and RgCl(B,C,D) + C_6F_5 systems. The RgCl(D) state correlates to the $Rg^+(^2P_{1/2})$ + Cl^- ion pair, while the RgCl(B,C) states correlate to the $Rg^+(^2P_{3/2})$ + Cl^- ion pair based upon ab initio calculations.[16-18]

There are quasi continuous Rg + C_6F_5Cl* (excited states) product channels below the $V[Rg^+,C_6F_5Cl^-]$ ion-pair potentials for a relatively large molecule such as C_6F_5Cl. Here, excited states of C_6F_5Cl involve superexcited states above the first ionization potential of 9.72 eV. In addition to the Rg + C_6F_5Cl* product channels, a number of Rg**(Rydberg states) + C_6F_5Cl potentials are present above the $Rg(^3P_{0,2})$ + C_6F_5Cl potentials as product channels, because the potential energies of $Rg^+(^2P_{3/2})$ + $C_6F_5Cl^-$ are higher than those of $Rg(^3P_0)$ + C_6F_5Cl by 1.9–3.3 eV. They are also shown by hatched lines in Fig. 7. In the $Ar^+(^2P_{1/2,3/2})/C_6F_5Cl^-$, $Kr^+(^2P_{1/2,3/2})/C_6F_5Cl^-$, and $Xe^+(^2P_{1/2,3/2})/C_6F_5Cl^-$ reactions, the following states exist as candidates for Rg** and some of them can interact with the entrance $V[Rg^+(^2P_{1/2,3/2}),C_6F_5Cl^-]$ ion-pair potentials: total 59 4*s*, 4*p*, 3*d*, 5*s*, 5*p*, 4*d*, 6*s*, and 4*f* states for Ar**, 51 5*s*, 5*p*, 4*d*, 6*s*, 6*p*, 5*d*, 7*s*, and 4*f* states for Kr**, and 48 6*s*, 6*p*, 5*d*, 7*s*, 7*p*, 6*d*, 8*s*, and 4*f* states for Xe**. As shown in Table 1, most of $Rg(^3P_{0,2})$/RX reactions give RgX* excimers via

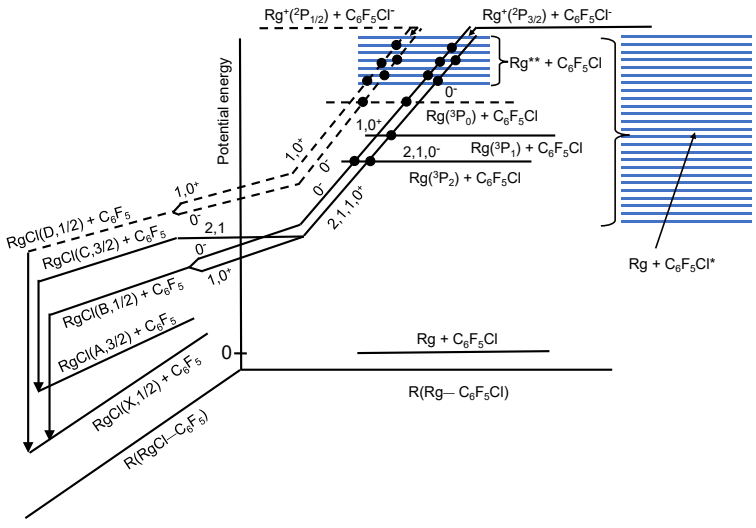

Fig. 7. Correlation diagram of the diabatic potentials for the $Rg(^3P_{0,2})/C_6F_5Cl$ and $Rg^+(^2P_{1/2,3/2})/C_6F_5Cl^-$ reactions. The states with $Rg^+(^2P_{1/2})$ ion-core configuration are shown by dashed lines. The dark circles show positions of strong interactions of the diabatic potentials. Ω values shown in Fig. A3 for the $Rg(^3P_{0,2})/X_2$ and $Rg^+(^2P_{1/2,3/2})/X_2^-$ reactions in collinear geometry are used.

$[Rg^+(^2P_{1/2,3/2}),RX^-]$ ion-pair intermediates. In the Xe**(6*p*,6*p*′,7*p*)/RX reactions,[22,23] XeX* excimer formation via $V[Xe^+(^2P_{1/2,3/2}),RX^-]$ ion-pair potentials has also been observed, indicating that higher energy entrance V[Xe**(6*p*,6*p*′,7*p*),RX] potentials really couple with the $V[Xe^+(^2P_{1/2,3/2}),RX^-]$ ion-pair potentials. If the attractive ion-pair potentials strongly couple with some of these $V[Rg,C_6F_5Cl^*]$ or V[Rg**,C_6F_5Cl] potentials, this coupling diverts trajectories from the ion-pair potential to the $V[Rg,C_6F_5Cl^*]$ or V[Rg**,C_6F_5Cl] potentials. The preferential formation of RgCl(D) from the $Rg^+(^2P_{1/2})/C_6F_5Cl^-$ reactions and the selective formation of RgF(B,C) from the $Rg^+(^2P_{3/2})/C_6F_5Cl^-$ reactions imply that trajectory loss by interactions with $V[Rg,C_6F_5Cl^*]$ or V[Rg**,C_6F_5Cl] potentials is small, so that the RgCl* excimers could be formed through diabatic pathways predicted from the potential diagram.

$$Rg^+(^2P_{1/2}) + C_6F_5Cl^- \rightarrow [Rg^+(^2P_{1/2}),Cl^-] + C_6F_5, \quad \downarrow \quad RgCl(D). \qquad (21a)$$

$$Rg^+(^2P_{3/2}) + C_6F_5Cl^- \rightarrow [Rg^+(^2P_{3/2}),Cl^-] + C_6F_5, \quad \downarrow \quad RgCl(B,C). \qquad (21b)$$

On the basis of this finding, the electronic configuration of rare gas ion is conserved well during the $Rg^+(^2P_{1/2,3/2})/C_6F_5Cl^-$ reactions.

The formation of a small amount of RgCl(B) from the $Rg^+(^2P_{1/2})/C_6F_5Cl^-$ reaction suggests that the conservation of ion configuration is partially broken. One possible route for the formation of RgCl(B) from the $Rg^+(^2P_{1/2})/C_6F_5Cl^-$ reaction shown in Fig. 7 is the first curve crossing between the $\Omega = 0^-$ entrance $V[Rg^+(^2P_{1/2}),C_6F_5Cl^-]$ potential and the $\Omega = 0^-$ potential arising from $Rg(^3P_0) + C_6F_5Cl$ followed by the second curve crossing between the $\Omega = 0^-$ potential from $Rg(^3P_0) + C_6F_5Cl$ and the $\Omega = 0^-$ potential arising from $Rg^+(^2P_{3/2}) + C_6F_5Cl^-$.

$$Rg^+(^2P_{1/2}) + C_6F_5Cl^- \rightarrow [Rg^+(^2P_{1/2}),C_6F_5Cl^-], \quad \downarrow \quad [Rg(^3P_0),C_6F_5Cl], \quad \downarrow \quad [Rg^+(^2P_{3/2}),C_6F_5Cl^-], \quad \downarrow \quad RgCl(B) + C_6F_5. \qquad (22)$$

Other possibilities are similar interactions between the entrance $V[Rg^+(^2P_{1/2}),RX^-]$ potential and some V[Rg**,RX] potential followed by interaction between V[Rg**,RX] and $V[Rg^+(^2P_{3/2}),RX^-]$ potentials.

The smaller Γ(D) values in the $Ar^+(^2P_{1/2})/C_6F_5Cl^-$ and $Xe^+(^2P_{1/2})/C_6F_5Cl^-$ reactions than that in the $Kr^+(^2P_{1/2})/C_6F_5Cl^-$ reaction suggest that conversion of ion-core configuration via curve crossings occurs with higher probability in the former reactions.

The spin-orbit state selectivity for the excimer formation in the reactions of metastable $Rg(^3P_{0,2})$ atoms with RX has been studied by Setser and his co-workers.[5-7] They discussed the electronic state selectivity of RgX* excimer in the $Rg(^3P_{0,2})$ reactions by both the *J* state and the ion core. As an example, Figure A3 in Appendix shows a schematic diagram of the RgX* formation from the $Rg(^3P_{0,2})/X_2$ reactions obtained by assuming a collinear approach. A similar potential diagram will be applicable to the formation of RgX* from the other $Rg(^3P_{0,2})$/RX reactions with a lower molecular symmetry. The formation of RgX* by the $Rg(^3P_{0,2})/X_2$ reactions proceeds through harpoon-type reactions via $[Rg^+,X_2^-]$ ion-pair intermediates. The metastable $Rg(^3P_0)$ and $Rg(^3P_2)$ atoms have $Rg^+(^2P_{1/2})$ and $Rg^+(^2P_{3/2})$ ion cores, respectively. If the ion-core configurations of $Rg(^3P_0)$ and $Rg(^3P_2)$ are conserved, the $Rg(^3P_0)$ atoms should yield the RgX(D) state through an $[Rg^+(^2P_{1/2}),X_2^-]$ intermediate, whereas the RgX(B,C) states would be formed through an $[Rg^+(^2P_{3/2}),X_2^-]$ intermediate.

$$Rg(^3P_0) + X_2 \rightarrow [Rg^+(^2P_{1/2}),X_2^-], \quad \downarrow \quad RgX(D) + X. \qquad (23a)$$

$$Rg(^3P_2) + X_2 \rightarrow [Rg^+(^2P_{2/2}),X_2^-], \quad \downarrow \quad RgX(B,C) + X. \qquad (23b)$$

Thus, the formation of D state from the $Rg(^3P_0)/X_2$ reactions and the B and C states from the $Rg(^3P_2)/X_2$ reactions has been explained by the conservation of ion-core configurations. The formation of B from the $Rg(^3P_0)$ reactions, which does not conserve the ion-core configuration, was attributed to a crossing between the $\Omega = 0^-$ entrance $V[Rg(^3P_0),X_2]$ potential and the $\Omega = 0^-$ $V[Rg^+(^2P_{3/2}),X_2^-]$ potential. In the $Rg(^3P_0)/X_2$ reactions, the crossing between the entrance $\Omega = 0^-$ potential and the outer $\Omega = 0^-$

$V[Rg^+(^2P_{3/2}),X_2^-]$ potential occurs before the formation of the $[Rg^+(^2P_{1/2}),X_2^-]$ intermediate. Therefore, for the formation of RgX(D) state, trajectories via $V[Rg(^3P_0),X_2]$ potential must pass through the outer crossing with the $V[Rg^+(^2P_{3/2}),X_2^-]$ potential and continue to the inner $V[Rg^+(^2P_{1/2}),X_2^-]$ potential.

In general, this diagram can also be applied to RX reagents as shown in Fig 7 for C_6F_5Cl. It should be noted that such an outer crossing is unnecessary for the formation of $[Rg^+(^2P_{1/2}),RX^-]$ intermediate in the $Rg^+(^2P_{1/2})/RX^-$ ionic-recombination reactions. Therefore, loss of initial trajectories by outer crossing is absent, so that a high propensity for the formation of RgCl(D) can be achieved in the $Rg^+(^2P_{1/2})/C_6F_5Cl^-$ reactions in comparison with that in the $Rg(^3P_0)/RX$ reaction. Higher propensity of RgX*(D) is especially found in the $Xe^+(^2P_{1/2})/C_6F_5Cl^-$ reaction in comparison with that in the $Xe(^3P_0)/RX$ reactions (Table 1). Zong et al.[7] attributed the low propensity of RgX*(D) in the $Xe(^3P_0)/RX$ reactions to a coupling between the $V[Xe(6s'^3P_0),RX]$ and $V[Xe(6p),RX]$ potentials in the entrance channel, because the emission spectra and the product branching ratios for XeX(B) formation from the reactions of $Xe(^3P_0)$ with RX molecules are similar to those from reactions of Xe(6*p*) atoms. The covalent $V[Xe(6s'\,^3P_0),RX]$ and $V[Xe(6p),RX]$ potentials are rather flat before crossing with strongly attractive ion-pair $V[Xe^+(^2P_{1/2}),RX^-]$ potential as reported by Nelson et al.[22] The $V[Xe(6p),RX]$ potentials are located at least 0.13 eV above the $V[Xe(6s'\,^3P_0),RX]$ potential. It is therefore expected that coupling between the $V[Xe(6s'\,^3P_0),RX]$ and $V[Xe(6p),RX]$ potentials in the entrance channel is weak at thermal energy. On the basis of present results, ion configuration is rather well conserved in the $Xe^+(^2P_{1/2})/C_6F_5Cl^-$ reaction, even though the entrance $V[Xe^+(^2P_{1/2}),C_6F_5Cl^-]$ potential can couple with many $V[Xe^{**},C_6F_5Cl]$ potentials involving $V[Xe(6p),C_6F_5Cl]$ potential. It is therefore reasonable to assume that the low propensity of RgX*(D) in the $Xe(^3P_0)/RX$ reactions arises from strong coupling of the entrance $\Omega = 0^-$ (A″) $V[Xe(^3P_0),RX]$ potential with outer $\Omega = 0^-$ (A″) $V[Xe^+(^2P_{3/2}),RX^-]$ potential.

In the $Ar(^3P_{0,2})/C_6F_5Cl$ reactions, no ArCl(B,C,D) formation was observed, even though they are energetically allowed. One possibility is the main product channel is Penning ionization leading to $C_6F_5Cl^+$, because the ionization potential of C_6F_5Cl (9.72 eV) is lower than energies of $Ar(^3P_2$:11.55 eV, $^3P_0$:11.72 eV).

$$Ar(^3P_{0,2}) + C_6F_5Cl \rightarrow C_6F_5Cl^+ + Ar + e^-. \quad (24)$$

Another possibility is that interactions of the entrance $V[Ar(^3P_{0,2}),C_6F_5Cl]$ potential with many low lying $V[Ar,C_6F_5Cl^*]$ potentials occur either directly or via $V[Ar^+(^2P_{1/2,3/2}),C_6F_5Cl^-]$ ion-pair potentials with high probability, so that no trajectories leading to ArCl* remain.

The conservation of ion configuration in the $Ar^+(^2P_{1/2})/C_6F_5Cl^-$ and $Xe^+(^2P_{1/2})/C_6F_5Cl^-$ reactions were smaller than that in the $Kr^+(^2P_{1/2})/C_6F_5Cl^-$ reaction. This suggests that interactions of entrance $V[Ar^+(^2P_{1/2}),C_6F_5Cl^-]$ and $V[Xe^+(^2P_{1/2}),C_6F_5Cl^-]$ potentials with $V[Ar^{**},C_6F_5Cl^-]$ and $V[Xe^{**},C_6F_5Cl^-]$ potentials, which divert the entrance trajectories, are stronger than that in the case of $Kr^+(^2P_{1/2})/C_6F_5Cl^-$ reaction.

4. Summary and Conclusion

Spin-orbit state selectivity of RgCl(B,C,D) excimers in the $Rg^+(^2P_{1/2,3/2})/C_6F_5Cl^-$ reactions was examined by selecting one spin-orbit component of $Rg^+(^2P_{1/2,3/2})$. The RgCl(B,D) ratio was determined to be 0.35:0.65, 0.05:0.95, and 0.24:0.76 in the $Ag^+(^2P_{1/2})$, $Kr^+(^2P_{1/2})$, and $Xe^+(^2P_{1/2})$ reactions, whereas the RgCl(B,C) ratio was estimated to be 0.74:0.26, 0.71:0.29, and 0.70:0.30 in the $Ag^+(^2P_{3/2})$, $Kr^+(^2P_{3/2})$, and $Xe^+(^2P_{3/2})$ reactions, respectively. The high propensities for the D formation from the $Rg^+(^2P_{1/2})/C_6F_5Cl^-$ reactions and for the B and C formation from the $Rg^+(^2P_{3/2})/C_6F_5Cl^-$ reactions could be explained by the conservation of the $Rg^+(^2P_{1/2}) + Cl^-$ and $Rg^+(^2P_{3/2}) + Cl^-$ characters for the formation of RgCl*. A high propensity for the formation of RgCl(D) in the $Rg^+(^2P_{1/2})/C_6F_5Cl^-$ reactions in comparison with that in the $Rg(^3P_0)/RX$ reactions was discussed by using a correlation diagram between entrance and exit product channels. In the $Rg(^3P_0)/RX$ reactions, the crossing between the entrance $\Omega = 0^-$ (A″) potential and the outer $\Omega = 0^-$ (A″) $V[Rg^+(^2P_{3/2}),RX^-]$ potential occurs before the formation of the $[Rg^+(^2P_{1/2}),RX^-]$ intermediate. Such a crossing is unnecessary for the formation of $[Rg^+(^2P_{1/2}),RX^-]$ intermediate in the ionic-recombination reactions. Therefore, a high propensity for the formation of RgCl(D) can be achieved in the $Rg^+(^2P_{1/2})/C_6F_5Cl^-$ reactions. The present results demonstrated the ionic recombination is better reaction for the selective formation of

RgX(D) excimers than the chemiluminescent reactions by the metastable $Rg(^3P_0)$ atoms.

Acknowledgments

The authors acknowledge Prof. Kenji Furuya of Kyushu University for his careful reading of our manuscript. This work has been supported by the Morino Foundation for molecular science (1992), the Iwatani Naoji Memorial Foundation (1993), and Showa Shell Sekiyu Foundation for environmental research (1995).

References

1) M. Tsuji, M. Furusawa, and Y. Nishimura, *Chem. Phys. Lett.*, 166, 363 (1990).
2) M. Tsuji, M. Furusawa, H. Kouno, and Y. Nishimura, *J. Chem. Phys.*, 94, 4291 (1991).
3) M. Tsuji, *Trends Phys. Chem.*, 5, 25 (1995).
4) M. Tsuji, *Houshasenkagaku*, 62, 18 (1996).
5) N. Sadeghi, M. Cheaib, and D. W. Setser, *J. Chem. Phys.*, 90, 219 (1989).
6) D. Zhong, D. W. Setser, R. Sobczynski, and W. Gadomski, *J. Chem. Phys.*, 105, 5020 (1992).
7) D. Zhong and D. W. Setser, *Chem. Phys. Lett.*, 207, 555 (1993).
8) A. L. Schmeltekopf and F. C. Fehsenfeld, *J. Chem. Phys.*, 53, 2000 (1970).
9) T. M. Miller and A. A. Viggiano, *Phys. Rev. A*, 71, 012702 (2005).
10) A. B. Rakshit and P. Warneck, *J. Chem. Phys.*, 73, 2673 (1980).
11) K. Giles, N. G. Adams, and D. Smith, *J. Phys. B*, 22, 873 (1983).
12) C. E. Moore, "*Atomic Energy Levels*," U.S. GPO, Washington D.C., *Natl. Bur. Stand.* (U.S.) Circ. 467 (1949).
13) *Atomic Spectra Database*, *NIST Standard Reference Database*, 78, Ver. 5.9. Oct. (2021).
14) Y.-R. Luo, "*Bond Dissociation Energies*", in *CRC Handbook of Chemistry and Physics*, 81th Ed., CRC Press, Boca Raton (2000).
15) *NIST Chemistry WebBook*, *NIST Standard Reference Database*, Number 69 (2022) https://doi.org/10.18434/T4D303
16) P. J. Hay and T. H. Dunning, *J. Chem. Phys.*, 66, 1306 (1977).
17) T. H. Dunning and P. J. Hay, *J. Chem. Phys.*, 69, 134 (1978).
18) P. J. Hay and T. H. Dunning, *J. Chem. Phys.*, 69, 2209 (1978).
19) T. D. Nguyen and N. Sadeghi, *Chem. Phys.*, 79, 41 (1983).
20) J. Derouard, T. D. Nguyen, and N. Sadeghi, *J. Chem. Phys.*, 72, 6698 (1980).
21) C. E. Brion, C. A. McDowell, and W. B. Stewart, *J. Electron Spectrosc.*, 1, 113 (1972/73).
22) T. O. Nelson, D. W. Setser, and K. Richmann, *J. Phys. Chem.*, 99, 7482 (1995).
23) V. Alekseev and D. W. Setser, *J. Phys. Chem.,* 100, 5766 (1996).

Appendix

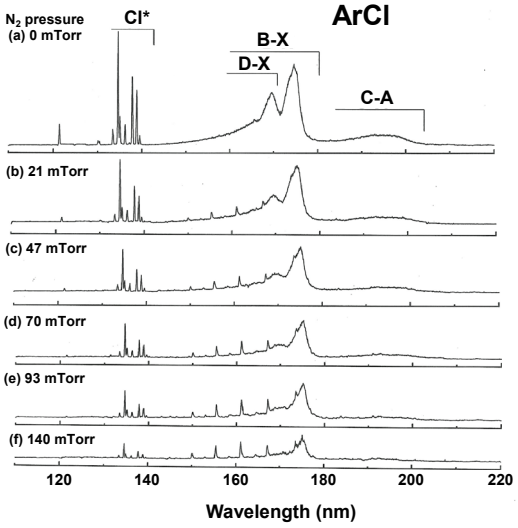

Fig. A1. Effects of N_2 addition to the emission spectra of ArCl* resulting from the $Ar^+(^2P_{1/2,3/2})/C_6F_5Cl^-$ reaction in the Ar afterglow.

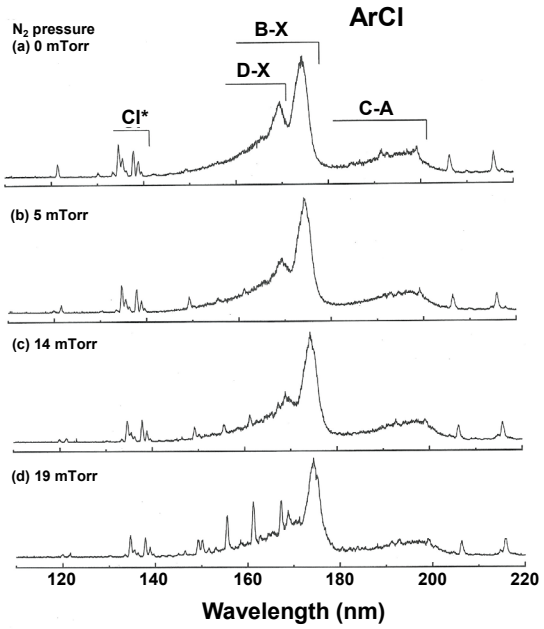

Fig. A2. Effects of N_2 addition to the emission spectra of ArCl* resulting from the $Ar^+(^2P_{1/2,3/2})/C_6F_5Cl^-$ reaction in the He afterglow.

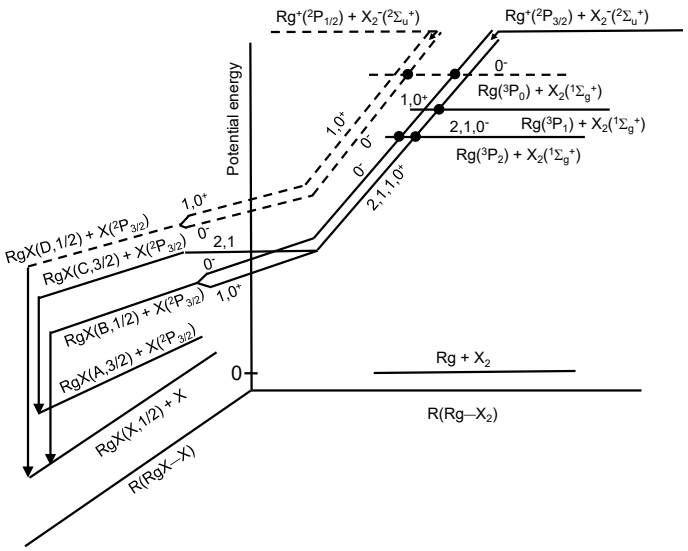

Fig. A3. Correlation diagram of the diabatic potentials for the $Rg(^3P_{0,2})/X_2$ and $Rg^+(^2P_{1/2,3/2})/X_2^-$ reactions in collinear geometry.[5] The states with $Rg^+(^2P_{1/2})$ ion-core configuration are shown by dashed lines. The dark circles show positions of expected strong interactions of the diabatic potentials. The only $\Omega = 1/2$ components correlating to $X(^2P_{3/2})$ have been included in the drawing because they are more important than $\Omega = 3/2$ components.